Article

# Spin splitting of dopant edge state in magnetic zigzag graphene nanoribbons

https://doi.org/10.1038/s41586-021-04201-y

Received: 18 April 2021

Accepted: 2 November 2021

Published online: 22 December 2021

Check for updates

Raymond E. Blackwell[1,5], Fangzhou Zhao[2,3,5], Erin Brooks[1], Junmian Zhu[1], Ilya Piskun[1], Shenkai Wang[1], Aidan Delgado[1], Yea-Lee Lee[2], Steven G. Louie[2,3]✉ & Felix R. Fischer[1,3,4]✉

Spin-ordered electronic states in hydrogen-terminated zigzag nanographene give rise to magnetic quantum phenomena[1,2] that have sparked renewed interest in carbon-based spintronics[3,4]. Zigzag graphene nanoribbons (ZGNRs)—quasi one-dimensional semiconducting strips of graphene bounded by parallel zigzag edges—host intrinsic electronic edge states that are ferromagnetically ordered along the edges of the ribbon and antiferromagnetically coupled across its width[1,2,5]. Despite recent advances in the bottom-up synthesis of GNRs featuring symmetry protected topological phases[6–8] and even metallic zero mode bands[9], the unique magnetic edge structure of ZGNRs has long been obscured from direct observation by a strong hybridization of the zigzag edge states with the surface states of the underlying support[10–15]. Here, we present a general technique to thermodynamically stabilize and electronically decouple the highly reactive spin-polarized edge states by introducing a superlattice of substitutional N-atom dopants along the edges of a ZGNR. First-principles GW calculations and scanning tunnelling spectroscopy reveal a giant spin splitting of low-lying nitrogen lone-pair flat bands by an exchange field (~850 tesla) induced by the ferromagnetically ordered edge states of ZGNRs. Our findings directly corroborate the nature of the predicted emergent magnetic order in ZGNRs and provide a robust platform for their exploration and functional integration into nanoscale sensing and logic devices[15–21].

Graphene nanostructures terminated by zigzag edges host spin-ordered electronic states that give rise to quantum magnetism[1,2]. These intrinsic magnetic states emerge from the zigzag edge structure of graphene itself, and create opportunities for the exploration of carbon-based spintronics and qubits[22–24], paving the way for the realization of high-speed, low-power operation spin-logic devices for data storage and information processing[25–28]. The edge states of ZGNRs have been predicted to exhibit a ferromagnetic (parallel) alignment of spins along either edge of the ribbon while the spins on two opposing edges are antiferromagnetically coupled (antiparallel alignment)[1,2]. This unusual electronic structure can give rise to field- or strain-driven half metallicity in ZGNRs[2,29]. A strong hybridization of the electronic edge states of ZGNRs with those of the underlying support, along with the susceptibility of zigzag edges to undergo passivation through atom-abstraction or radical-recombination reactions, represents a veritable challenge to their exploration[30].

Our strategy for engineering robust ZGNR edge states relies on the introduction of a superlattice of isoelectronic substitutional dopant atoms along both edges of a ZGNR. Replacement of every sixth C–H group along the zigzag edge of a 6-ZGNR (a zigzag GNR featuring six lines of carbon atoms across the width of the ribbon) by a N atom leads to the structure of N-6-ZGNRs depicted in Fig. 1a. Each trigonal planar N atom contributes the same number of electrons (one electron in a half-filled $p_z$-orbital) to the extended π-system of the N-6-ZGNR as the trigonal planar C–H groups that they replace. Although the magnetic spin-polarized edge states remain largely unaffected by the subtle modulation of frontier bands imposed by a superlattice of N-dopant atoms, first-principles calculations show that the substitutional doping in N-6-ZGNRs leads to a lowering of the total energy of formation ($E_f$) by $\Delta E_f = -0.124$ eV per unit cell when compared to the parent 6-ZGNRs (see Methods).

Guided by this idea we designed a molecular precursor for N-6-ZGNRs, the dibenzoacridine **1** (Fig. 1b). N-6-ZGNRs were grown on Au(111) films on mica by sublimation of **1** in ultrahigh vacuum (UHV) onto a clean Au(111) surface held at 297 K. Fig. 1c shows a constant-current scanning tunnelling microscopy (STM) topographic image of a sub-monolayer coverage of **1** on Au(111) at $T = 4$ K. Molecule-decorated surfaces were subsequently annealed at 475 K to induce the homolytic cleavage of C–Br bonds followed by a radical step-growth polymerization to give *poly*-**1**. Further annealing at 650 K induces a thermal cyclodehydrogenation that leads to the fully fused N-6-ZGNR backbone (Fig. 1d). STM topographic images reveal extended GNRs featuring atomically smooth zigzag edges with an apparent height and width of 0.23 nm ± 0.03 nm and 1.95 nm ± 0.05 nm, respectively, consistent with the formation of the fully conjugated N-6-ZGNR backbone (Extended Data Fig. 1). The position of N atoms along the edges of N-6-ZGNRs can be

[1]Department of Chemistry, University of California, Berkeley, CA, USA. [2]Department of Physics, University of California, Berkeley, CA, USA. [3]Materials Sciences Division, Lawrence Berkeley National Laboratory, Berkeley, CA, USA. [4]Kavli Energy NanoScience Institute at the University of California Berkeley and the Lawrence Berkeley National Laboratory, Berkeley, CA, USA. [5]These authors contributed equally: Raymond E. Blackwell, Fangzhou Zhao. ✉e-mail: sglouie@berkeley.edu; ffischer@berkeley.edu

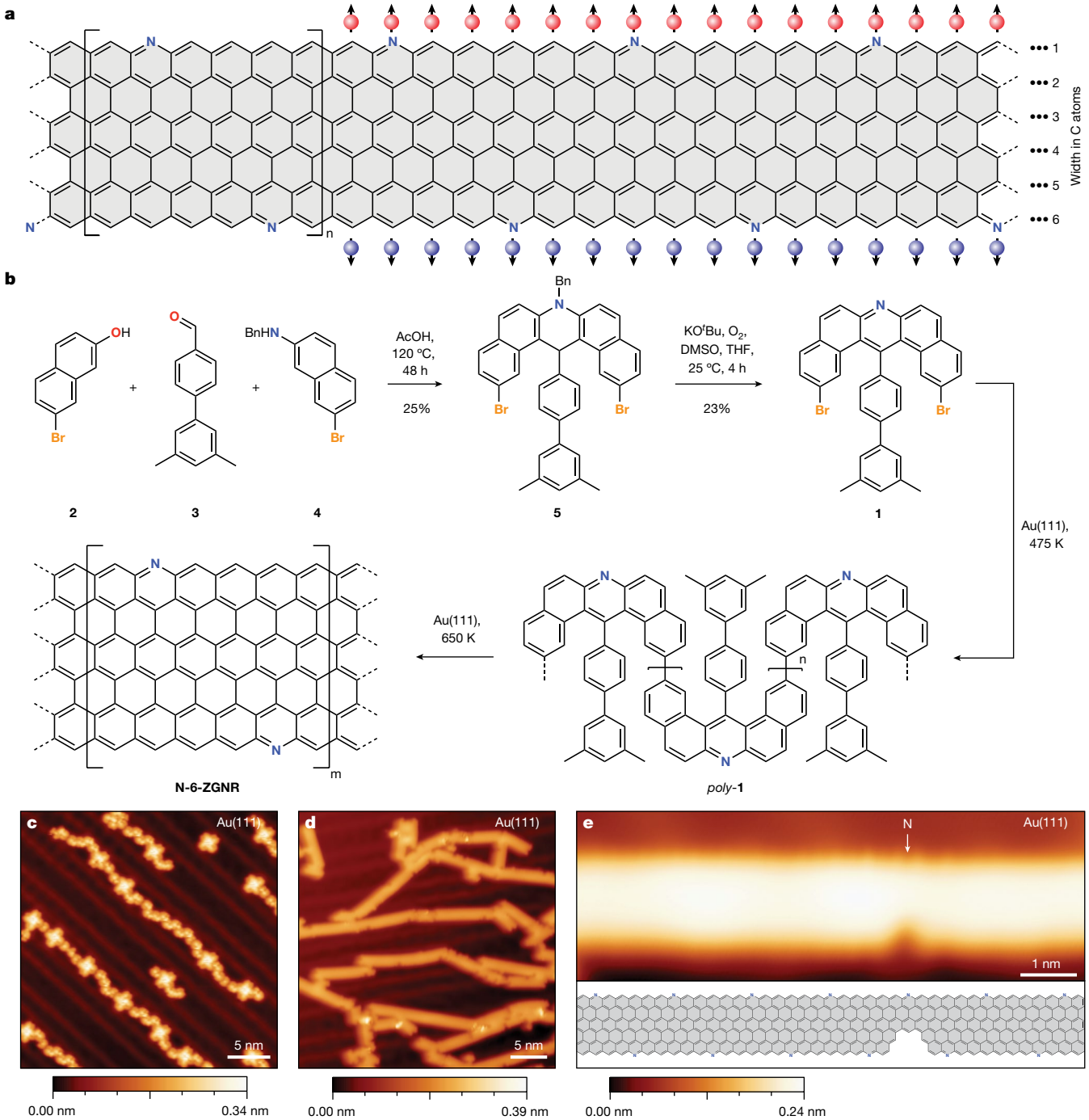


**Fig. 1 | Bottom-up synthesis of N-doped N-6-ZGNRs. a**, Schematic representation of spin-ordered edge states in N-6-ZGNRs. **b**, Schematic representation of the bottom-up synthesis and on-surface growth of N-6-ZGNRs from molecular precursor **1**. **c**, STM topographic image of molecular precursor **1** as deposited on Au(111) ($V_s$ = 50 mV, $I_t$ = 20 pA). **d**, STM topographic image of fully cyclized N-6-ZGNRs following annealing to 650 K ($V_s$ = 50 mV, $I_t$ = 20 pA). **e**, STM topographic image of a fully cyclized N-6-ZGNR featuring a characteristic single point defect resulting from the cleavage of an *m*-xylene group ($V_s$ = 50 mV, $I_t$ = 20 pA). Arrow, position of a N atom. Inset, chemical structure of the N-6-ZGNR segment imaged in **e**. All STM images recorded at $T$ = 4 K. DMSO, dimethylsulfoxide ; THF, tetrahydrofuran.

inferred from a characteristic edge defect previously observed for all-carbon 6-ZGNRs[15]. Excision of a *m*-xylyl group in *poly*-**1** during the thermal cyclodehydrogenation step results in an indentation along the zigzag edge of the GNR (Fig. 1e, inset). The position of a N-dopant atom at the opposing zigzag edge across from the defect site can be derived directly from the structure of the molecular building block **1**.

Topographic (Fig. 2a) and bond-resolved STM (BRSTM) images (Fig. 2b) were recorded on a fully cyclized segment of N-6-ZGNR featuring the same *m*-xylyl deletion defect. Although topographic STM images (Fig. 2a) resolve the zigzag edge structure of N-6-ZGNRs and hint at a superlattice of substitutional N dopants, BRSTM images show an alternating pattern of five bright lobes protruding from the edge of the N-6-ZGNRs (Fig. 2b, arrows) flanked on either side by indentations of darker contrast. The pattern on one zigzag edge is offset by half a period from the opposite edge and is superimposable with the position of N atoms derived from the analysis of *m*-xylyl deletion defects. Enhanced signal in zero-bias d*I*/d*V* imaging suggests a strong hybridization of the Au(111) surface state with the spin-polarized edge

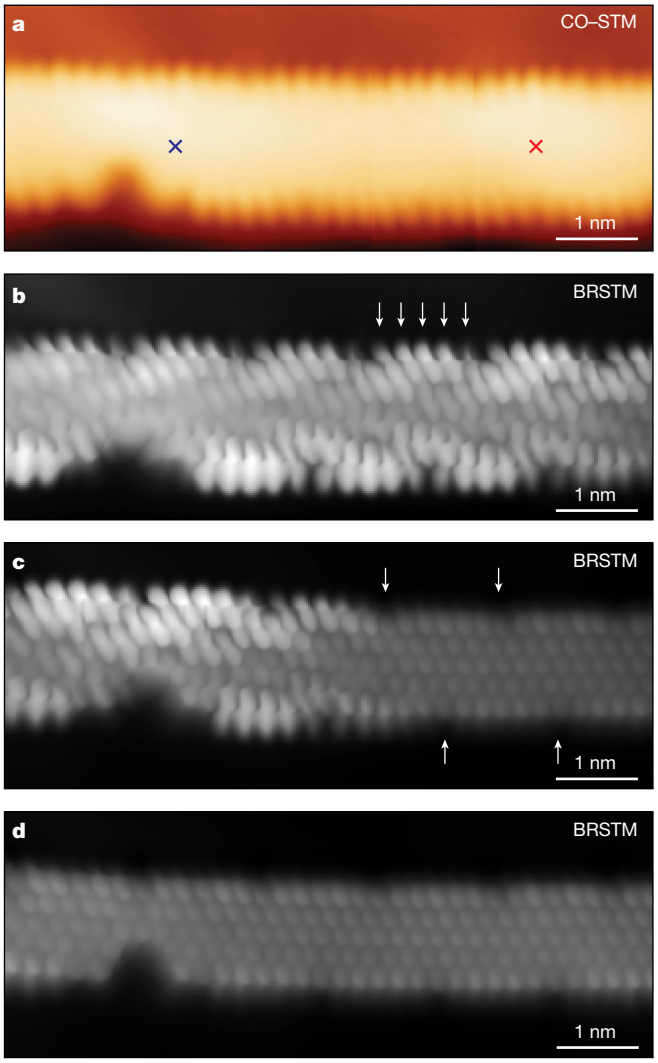


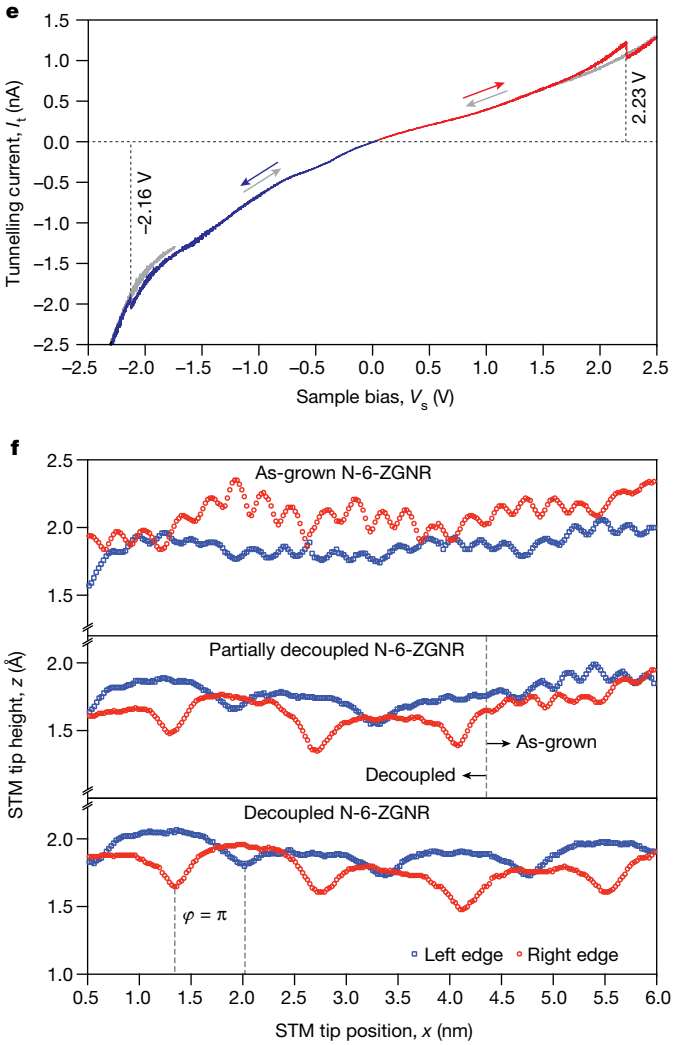


**Fig. 2 | Tip-induced decoupling of magnetic edge states in N-6-ZGNRs from Au surface. a**, Topographic image of a fully cyclized N-6-ZGNR segment recorded with a CO-functionalized STM tip. **b**, Constant-height BRSTM image of the N-6-ZGNR segment from **a**. Arrows, position of the five lobes associated with the C–H groups along the edges of the N-6-ZGNR ($V_s$ = 0 mV, modulation voltage $V_{ac}$ = 11 mV, modulation frequency $f$ = 455 Hz). **c**, Constant-height BRSTM image of N-6-ZGNR segment following tip-induced decoupling using a positive voltage sweep from $V_s$ = 0.0 V to $V_s$ = +2.5 V at the position marked by a red cross in **a** ($V_s$ = 0 mV, $V_{ac}$ = 11 mV, $f$ = 455 Hz). Arrows, position of selected N atoms along the edge of the N-6-ZGNR. **d**, BRSTM image of N-6-ZGNR segment following tip-induced decoupling using a negative voltage sweep from $V_s$ = 0.0 V to $V_s$ = −2.5 V at the position marked by a blue cross in **a** following decoupling in **c** ($V_s$ = 0 mV, $V_{ac}$ = 11 mV, $f$ = 455 Hz). **e**, $I_t/V_s$ plot showing the positive (red) and negative (blue) voltage sweeps used during the decoupling procedure. Return sweeps (grey) show the irreversible shift in the tunnelling current $I_t$. **f**, STM height profiles showing the corrugation recorded along the left edge (blue squares) and the right edge (red circles) of a representative as-grown N-6-ZGNR (top), a partially decoupled N-6-ZGNR (middle), and a fully decoupled N-6-ZGNR (bottom) ($V_s$ = 50 mV, $I_t$ = 20 pA; CO-functionalized tip). All STM experiments performed at $T$ = 4 K.

states of the ribbon. d$I$/d$V$ point spectra recorded along the edges of as-grown N-6-ZGNRs (as-grown herein refers to GNRs that have not been subjected to STM tip-induced decoupling) show a broad featureless local density of states (LDOS) that cannot be assigned to van Hove singularities associated with the valence band and conduction band edge (Fig. 3a and Extended Data Fig. 2b).

To overcome this robust electronic coupling and experimentally access magnetic edge states of ZGNRs, we developed a scanning probe microscopy (SPM) tip-induced decoupling protocol that disrupts the strong hybridization of the N-6-ZGNRs with Au(111). When placing the STM tip ~4 Å above the centre of a N-6-ZGNR (Fig. 2a, red cross), and sweeping the bias voltage from $V_s$ = 0.00 V to $V_s$ = +2.50 V, a discontinuous drop in the tunnelling current ($\Delta I_t^+$ = 0.16 nA) can be observed at $V_s^+$ = +2.23 ± 0.05 V (Fig. 2e and Extended Data Fig. 3). The abrupt decrease in $I_t$ suggests an electronic decoupling of the GNR from the underlying Au(111) substrate. Subsequent bias sweeps from $V_s$ = 0.00 V to +2.50 V near the position of the red cross yield no further change in $I_t$. STM imaging of the same N-6-ZGNR segment following tip-induced decoupling reveals a local change in the constant-height d$I$/d$V$ map (Extended Data Fig. 4). BRSTM images (Fig. 2c) of the ribbon in the vicinity of the STM tip during the decoupling step (1–2 nm surrounding the position of the red cross) are clearly resolved and show the distinctive structure of the N-6-ZGNR backbone and the characteristic pattern of N atoms along both zigzag edges (Fig. 2c, arrows, N atoms appear with a darker contrast when compared to the C–H groups; Extended Data Fig. 5a, b). The same irreversible decoupling event can be observed by applying a negative bias. Sweeping the bias voltage from $V_s$ = 0.00 V to $V_s$ = −2.50 V (Fig. 2a, blue cross) reveals a comparable drop $\Delta I_t^-$ = 0.15 nA at $V_s^-$ = −2.16 ± 0.05 V. The resulting BRSTM images (Fig. 2d) show the bond-resolved structure of the N-6-ZGNR backbone along the entire length of the ribbon. Neighbouring ribbons that are not covalently fused with the N-6-ZGNR subjected to the decoupling protocol remain unaffected by this process (Extended Data Fig. 5c, d).

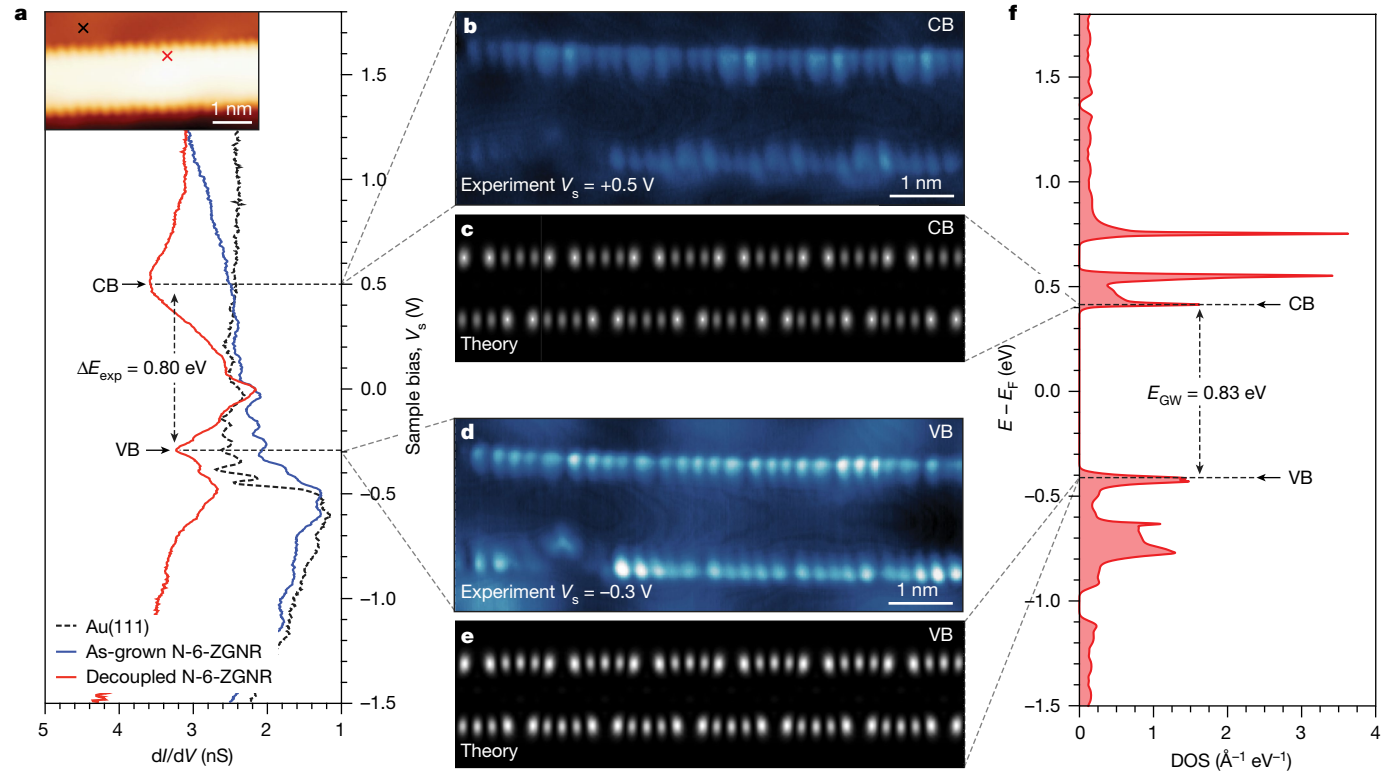


**Fig. 3 | Electronic structure of N-6-ZGNR. a**, d*I*/d*V* point spectroscopy of as-grown (blue) and decoupled (red) N-6-ZGNR/Au(111) at the position marked in the inset (red cross; imaging, $V_s = 50$ mV, $I_t = 20$ pA, CO-functionalized tip); Au(111) reference spectrum (black) (spectroscopy, $V_{ac} = 11$ mV, $f = 455$ Hz). **b**, Constant-current d*I*/d*V* map recorded at a voltage bias of $V_s = +0.5$ V ($V_{ac} = 11$ mV, $I_t = 200$ pA, $f = 455$ Hz, CO-functionalized tip). **c**, Calculated GW LDOS at the conduction band (CB) edge. **d**, Constant-current d*I*/d*V* map recorded at a voltage bias of $V_s = -0.3$ V ($V_{ac} = 11$ mV, $I_t = 170$ pA, $f = 455$ Hz, CO-functionalized tip). **e**, Calculated GW LDOS at the valence band (VB) edge. **f**, Calculated GW DOS for a N-6-ZGNR (spectrum broadened by 4 meV Gaussian). All STM experiments were performed at $T = 4$ K. Theoretical LDOS are sampled at a height of 4 Å above the atomic plane of the N-6-ZGNR.

The mechanism of this electronic decoupling can be explained by a tip-induced relaxation of the adsorption geometry of N-6-ZGNRs on Au(111). STM height profiles recorded along opposing zigzag edges of as-grown N-6-ZGNRs (Fig. 2f, top) are characterized by irregular π-bonding interaction patterns between the Au(111) surface layer and C and N atoms lining the edges of the ribbon (Extended Data Fig. 6). Local application of our SPM tip-induced decoupling protocol reversibly breaks C–Au and N–Au π-bonds allowing the backbone of N-6-ZGNRs to adopt a less strained, lower energy adsorption geometry epitaxial with respect to the Au(111) surface (Extended Data Fig. 6c). STM line profiles of partially and fully decoupled N-6-ZGNRs (Fig. 2f) show that this global minimum adsorption geometry is characterized by a height modulation ($\Delta z \sim 0.3$ Å) along the edges of the ribbon that places N atoms closest to the Au(111) surface. The corrugation of opposing zigzag edges in decoupled N-6-ZGNRs is offset by half a period ($\varphi = \pi$) to fall in registry with the atomic spacing of the Au(111) surface layer. First-principles calculations confirm that this conformation represents the global minimum adsorption geometry of N-6-ZGNR on Au(111) (lattice commensuration between N-6-ZGNRs and Au(111) < 1.8%, see Extended Data Fig. 6).

The local electronic structure of surface-decoupled N-6-ZGNRs was characterized by d*I*/d*V* point spectroscopy. A typical d*I*/d*V* point spectrum recorded along the edge of N-6-ZGNRs (>3 nm from either end of the ribbon; Fig. 3a, inset) shows two prominent electronic states. A sharp peak centred at $V_s = -0.30 \pm 0.02$ V and a broader feature at $V_s = +0.50 \pm 0.05$ V can be assigned to the valence band and conduction band edge, respectively. Substitution of C–H groups with the more electronegative N atoms not only leads to an overall thermodynamic stabilization of N-6-ZGNRs but a significant reduction of the band gap, $\Delta E_{exp} = 0.80 \pm 0.05$ eV, when compared to a pristine all-carbon 6-ZGNR ($\Delta E_{GW} = 1.20$ eV) (Extended Data Fig. 7a). d*I*/d*V* imaging of the spatial distribution of the LDOS at energies close to the conduction band edge (Fig. 3b) shows the largest contrast along the zigzag edge C–H groups flanking the position of N-atom dopants while the intensity decreases toward the centre of the N-6-ZGNR backbone. d*I*/d*V* maps recorded at an imaging bias of −0.30 V reveal the LDOS associated with the valence band state (Fig. 3d) evenly distributed over the C–H groups lining the zigzag edges. Both d*I*/d*V* maps of the conduction band and valence band edge states show slightly weaker contrast at the position of the N-atom dopants, a prominent feature that creates the illusion of isolated pentacene-like motifs lining the edges of N-6-ZGNRs. Rather than invoking a localization of the extended conduction band and valence band edge states, the difference in contrast between C–H groups and N atoms in calculations is a consequence of the edge state extending further into the space above and below the N-6-ZGNR plane at the position of the C atoms than the site of the N atoms. The difference in the contrast between C–H groups and N atoms in d*I*/d*V* maps is further exaggerated by the corrugation of the zigzag edges in the preferred adsorption geometry of decoupled N-6-ZGNRs placing the N atoms closer to the Au(111) surface.

Experimental results are in agreement with theoretical calculations based on ab initio density functional theory (DFT) within the local spin density approximation (LSDA)[31], and ab initio GW calculations[32], which includes the important self-energy corrections to the quasiparticle excitations measured in STS experiments. Our first-principles results provide quantitative evidence that the SPM tip-induced decoupling has resulted in a full recovery of the intrinsic magnetic edge states (both in energy and wavefunction) of N-6-ZGNRs. Fig. 3c, e shows the calculated LDOS maps at a distance of 4 Å above the plane of the freestanding N-6-ZGNR at energies corresponding to the conduction

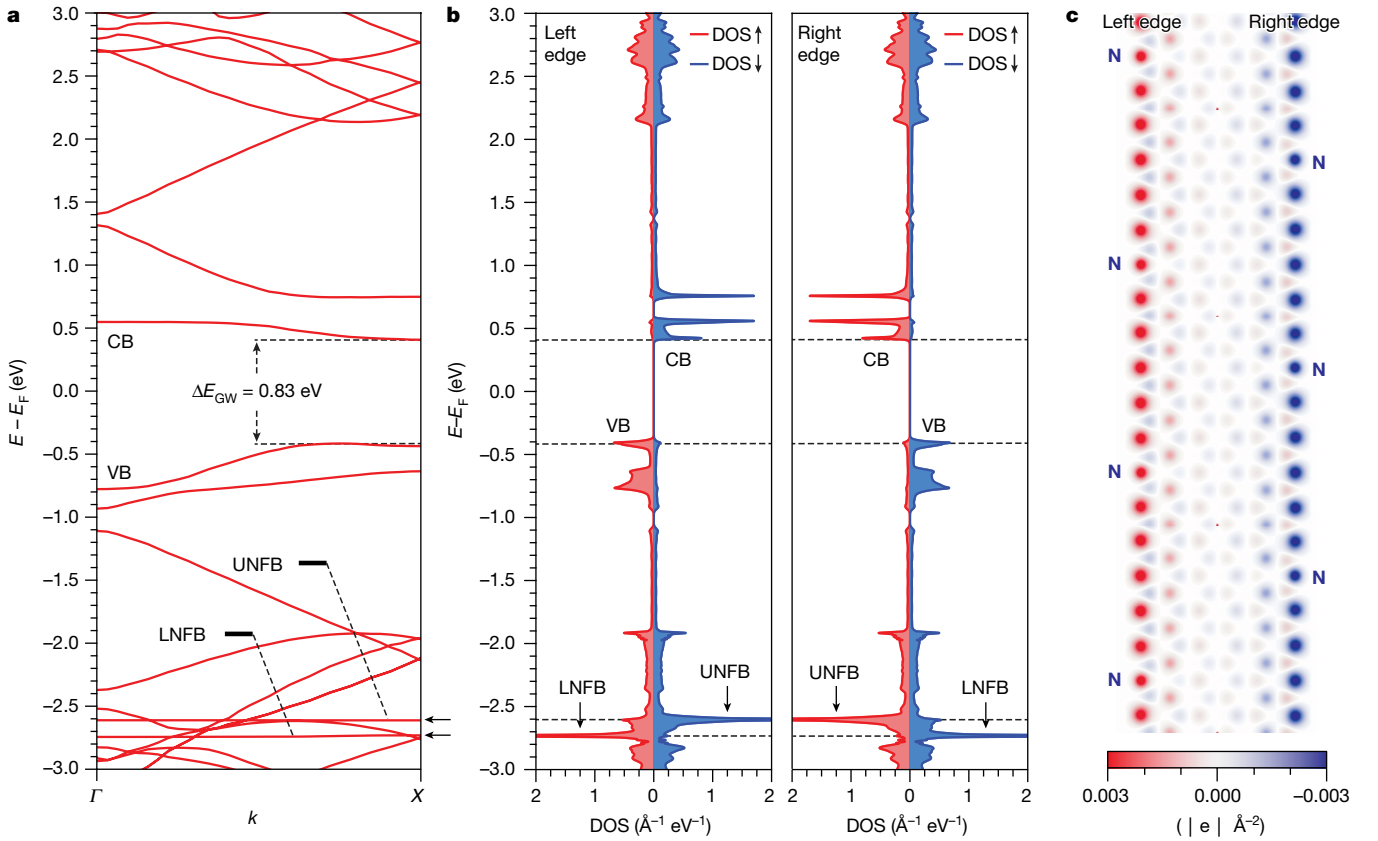


**Fig. 4 | Band structure and spatial distribution of spin-ordered edge states in N-6-ZGNRs. a**, GW band structure of a freestanding N-6-ZGNR. Upper (UNFB) and lower (LNFB) nitrogen flat bands are highlighted by arrows. **b**, GW LDOS of up (red) and down (blue) spin integrated over the left half and right half of a N-6-ZGNR as shown in **c**. **c**, Spatial distribution of the areal spin density distribution difference of the occupied states between up and down spin ($\rho_\uparrow(r) - \rho_\downarrow(r)$). The areal density is the density integrated in the direction out of the GNR atomic plane.

band and valence band edges. The characteristic pattern and relative contrast of protrusions lining the edges of N-6-ZGNRs (Fig. 3b, d) are faithfully reproduced in the corresponding GW LDOS maps (Fig. 3c, e). The GW band structure and the corresponding density of states (DOS) are depicted in Figs. 4a and 3f, respectively. The quasiparticle band-gap $\Delta E_{GW}$ = 0.83 eV, as defined in Fig. 3f, is in good agreement with the experimental gap $\Delta E_{exp}$ = 0.80 ± 0.05 eV derived from STS and implies the hybridization of N-6-ZGNRs with the underlying Au(111) substrate is significantly reduced in the global minimum adsorption geometry. Electronic coupling with the Au(111) surface state is weak as the LDOS along the *z*-axis associated with the spin-polarized valence band and conduction band edge states in N-6-ZGNRs is smallest at the position of the N atoms. The observation that the calculated peak-to-peak gap on N-6-ZGNRs remains slightly larger than the experimental value is owing to dielectric screening by the Au substrate.

Ab initio calculations on N-6-ZGNR show that an antiferromagnetic alignment of spins (across the ribbon width) between ferromagnetically ordered edge states (for example, as shown in Fig. 4c; left edge, up spin, and right edge, down spin; note that the absolute spin orientation is arbitrary due to negligible spin-orbit interactions) is favoured as the ground state over a spatially spin-unpolarized configuration. The spin-polarization energy is 16 meV per edge atom, indicating large magnetic interaction energies. The antiferromagnetic spin configuration in the ground state is consistent with Lieb's theorem for interacting electrons on a bipartite lattice[33]. The GW LDOS of upwards and downwards spin integrated over the left and right half of a N-6-ZGNR (Fig. 4b) shows the expected spatial distribution of the two spin species at the bottom conduction band and top valence band. Besides the obvious polarization of the frontier bands, our calculations predict two low-lying highly spatially localized spin-polarized states at $E - E_F$ = −2.60 eV and $E - E_F$ = −2.72 eV, respectively. These highly localized flat-band states are formed by the lone-pair orbitals of trigonal planar N atoms lining the edges of N-6-ZGNRs. The two bands (which have no splitting in spin-unpolarized calculations, Extended Data Fig. 7d) split into an upper nitrogen flat band (UNFB; −2.60 eV) and a lower nitrogen flat band (LNFB; −2.72 eV) due to the exchange interaction of the lone-pair electron with the spin-polarized π-electrons, which have a net spin population of opposite sign along the two edges. The exchange field generated by the ferromagnetic ordering on either N-6-ZGNR edge (corresponding to an effective Zeeman field of $B_{calc}$ ~ 1,000 T) favours a local spin orientation that is parallel to the local exchange field. The LNFB and UNFB with spatial spin polarization in the same (left edge, up spin; right edge, down spin) and opposite (left edge, down spin; right edge, up spin) direction as the magnetic ordering of the N-6-ZGNR edges are lowered and raised in energy, respectively, leading to a splitting of the flat nitrogen lone-pair bands.

To validate our theoretical predictions, we recorded d*I*/d*V* point spectra along the edge of a fully decoupled N-6-ZGNR at a bias from $V_s$ = −1.50 V to $V_s$ = −3.00 V (Extended Data Fig. 8). Only when the STM tip is located immediately above the position of a N atom (Fig. 5a), do the d*I*/d*V* point spectra show two characteristic peaks centred at $V_s$ = −2.60 ± 0.02 V and $V_s$ = −2.70 ± 0.02 V, corresponding to the UNFB and LNFB states, respectively (Extended Data Fig. 9). d*I*/d*V* imaging of the spatial distribution of the LDOS at energies close to the UNFB and LNFB reveals a featureless ZGNR backbone that shows enhanced contrast at the edge of the ribbon at the precise position of the N atoms (Fig. 5b, d and Extended Data Fig. 10). The distinctive patterns in the d*I*/d*V* maps faithfully reproduce the calculated UNFB and LNFB LDOS

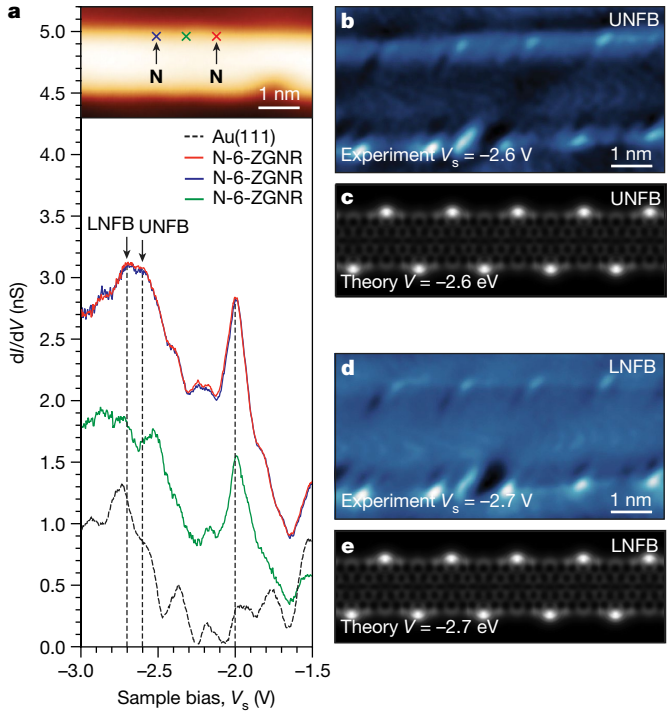


**Fig. 5 | Spin splitting of nitrogen flat band states (NFB) of $sp^2$ lone-pair orbitals in N-6-ZGNRs. a**, d$I$/d$V$ point spectroscopy of decoupled N-6-ZGNR on Au(111) at the position of two N atoms marked in the inset (red and blue cross; imaging, $V_s$ = 300 mV, $I_t$ = 20 pA), at the position of a carbon atom between the two N atoms (green cross); Au(111) reference spectrum (black) (spectroscopy, $V_{ac}$ = 11 mV, $f$ = 455 Hz). **b**, Constant-current d$I$/d$V$ map of UNFB recorded at a voltage bias of $V_s$ = −2.6 V ($V_{ac}$ = 11 mV, $I_t$ = 2 nA, $f$ = 455 Hz). **c**, Calculated GW LDOS integrated in a bias range $\Delta V$ = 200 mV around the UNFB. **d**, Constant-current d$I$/d$V$ map of LNFB recorded at a voltage bias of $V_s$ = −2.7 V ($V_{ac}$ = 11 mV, $I_t$ = 2 nA, $f$ = 455 Hz). **e**, Calculated GW LDOS integrated in a bias range $\Delta V$ = 200 mV around the LNFB.

maps (Fig. 5c, e), further corroborating the assignment of UNFB and LNFB to the spin-split nitrogen lone-pair bands.

Although the longitudinal modulation of the valence band and conduction band states imposed by a substitutional N-dopant superlattice represents a universal strategy to stabilize the exotic magnetic edge states in ZGNRs, the isoelectronic substitution of one out of six of the C–H groups along the zigzag edge with N atoms does not deteriorate the spin polarization and the edge magnetism in ZGNRs. Our calculated spatial distribution of electron spin polarization in the ground state (Fig. 4c) reveals that the magnetization on one N atom in N-6-ZGNRs amounts to ~80% of the expected magnetization of a C atom along the edge of a pristine 6-ZGNR, indicating almost unaltered magnetic edge states. The experimentally observed large exchange splitting $\Delta E_{STS}$ = 100 ± 30 meV of the low-lying nitrogen lone-pair dopant flat bands by the ferromagnetically ordered spins along the edge of N-6-ZGNRs implies that the two electrons occupying the nitrogen lone-pair experience an effective local exchange field $B_{eff}$ = 850 ± 250 T, consistent with theoretical prediction. We therefore conclude that the isoelectronic substitution of C–H groups with N-atom dopants does not disrupt the intrinsic magnetization emerging from the spin-polarized edge states in ZGNRs. Our results provide direct experimental evidence for the antiferromagnetic coupling of the ferromagnetically ordered edge states on opposite edges of ZGNRs. SPM tip-induced decoupling fully restores the emergent spin degree of freedom in N-6-ZGNRs and creates a path for the development of atomically precise graphene-based high-speed low-power spin-logic devices for data storage and information processing.

## Online content

Any methods, additional references, Nature Research reporting summaries, source data, extended data, supplementary information, acknowledgements, peer review information; details of author contributions and competing interests; and statements of data and code availability are available at https://doi.org/10.1038/s41586-021-04201-y.


1. Fujita, M., Wakabayashi, K., Nakada, K. & Kusakabe, K. Peculiar localized state at zigzag graphite edge. *J. Phys. Soc. Japan* **65**, 1920–1923 (1996).
2. Son, Y.-W., Cohen, M. L. & Louie, S. G. Half-metallic graphene nanoribbons. *Nature* **444**, 347–349 (2006).
3. Han, W., Kawakami, R. K., Gmitra, M. & Fabian, J. Graphene spintronics. *Nat. Nanotechnol.* **9**, 794–807 (2014).
4. Bullard, Z., Girao, E. C., Owens, J. R., Shelton, W. A. & Meunier, V. Improved all-carbon spintronic device design. *Sci. Rep.* **5**, 7634 (2015).
5. Yang, L., Park, C. -H., Son, Y. -W., Cohen, M. L. & Louie, S. G. Quasiparticle energies and band gaps in graphene nanoribbons. *Phys. Rev. Lett.* **99**, 186801 (2007).
6. Rizzo, D. J. et al. Topological band engineering of graphene nanoribbons. *Nature* **560**, 204–208 (2018).
7. Groning, O. et al. Engineering of robust topological quantum phases in graphene nanoribbons. *Nature* **560**, 209–213 (2018).
8. Cao, T., Zhao, F. Z. & Louie, S. G. Topological phases in graphene nanoribbons: junction states, spin centers, and quantum spin chains. *Phys. Rev. Lett.* **119**, 076401 (2017).
9. Rizzo, D. J. et al. Inducing metallicity in graphene nanoribbons via zero-mode superlattices. *Science* **369**, 1597–1603, (2020).
10. Lee, G. & Cho, K. Electronic structures of zigzag graphene nanoribbons with edge hydrogenation and oxidation. *Phys. Rev. B* **79**, 165440 (2009).
11. Ritter, K. A. & Lyding, J.W. The influence of edge structure on the electronic properties of graphene quantum dots and nanoribbons. *Nat. Mater.* **8**, 235–242 (2009).
12. Tao, C. et al. Spatially resolving edge states of chiral graphene nanoribbons. *Nat. Phys.* **7**, 616–620 (2011).
13. Li, Y. Y., Chen, M. X., Weinert, M. & Li, L. Direct experimental determination of onset of electron-electron interactions in gap opening of zigzag graphene nanoribbons. *Nat. Comm.* **5**, 4311 (2014).
14. Magda, G. Z. et al. Room-temperature magnetic order on zigzag edges of narrow graphene nanoribbons. *Nature* **514**, 608–611 (2014).
15. Ruffieux, P. et al. On-surface synthesis of graphene nanoribbons with zigzag edge topology. *Nature* **531**, 489–492 (2016).
16. Beyer, D. et al. Graphene nanoribbons derived from zigzag edge-encased poly(para-2,9-dibenzo[bc,kl]coronenylene) polymer chains. *J. Am. Chem. Soc.* **141**, 2843–2846 (2019).
17. Fu, Y. et al. On-surface synthesis of NBN-doped zigzag-edged graphene nanoribbons. *Angew. Chem. Int. Ed.* **59**, 8873–8879 (2020).
18. Li, Y., Zhou, Z., Cabrera, C. R. & Chen, Z. Preserving the edge magnetism of zigzag graphene nanoribbons by ethylene termination: insight by Clar's rule. *Sci. Rep.* **3**, 2030 (2013).
19. Shinde, P. P. et al. Stability of edge magnetism in functionalized zigzag graphene nanoribbons. *Carbon* **124**, 123–132 (2017).
20. Salemi, L., Lherbier, A. & Charlier, J. C. Spin-dependent properties in zigzag graphene nanoribbons with phenyl-edge defects. *Phys. Rev. B* **98**, 214204 (2018).
21. Lopez-Urias, F et al. Spin-dependent band-gap driven by nitrogen and oxygen functional groups in zigzag graphene nanoribbons. *Appl. Surf. Sci.* **521**, 146435 (2020).
22. Guo, G. -P. et al. Quantum computation with graphene nanoribbon. *New J. Phys.* **11**, 123005 (2009).
23. Luis, F. & Coronado, E. Spinning on the edge of graphene. *Nature* **557**, 645–647 (2018).
24. Mandal, B., Sarkar, S., Pramanik, A. & Sarkar, P. Doped defective graphene nanoribbons: a new class of materials with novel spin filtering properties. *RSC Adv.* **4**, 49946–49952 (2014).
25. Dery, H., Dalal, P., Cywinski, L. & Sham, L. J. Spin-based logic in semiconductors for reconfigurable large-scale circuits. *Nature* **447**, 573–576 (2007).
26. Dery, H. et al. Nanospintronics based on magnetologic gates. *IEEE Trans. Electron Devices* **59**, 259–262 (2012).
27. Lin, X., Yang, W., Wang, K. L. & Zhao, W. Two-dimensional spintronics for low-power electronics. *Nat. Electron.* **2**, 274–283 (2019).
28. Ahn, E. C., Wong, H. -S. P. & Pop, E. Carbon nanomaterials for non-volatile memories. *Nat. Rev. Mater.* **3**, 18009 (2018).
29. Zhang, D. -B. & Wei, S. -H. Inhomogeneous strain-induced half-metallicity in bent zigzag graphene nanoribbons. *NPJ Comput. Mater.* **3**, 32 (2017).
30. Berdonces-Layunta, A. et al. Chemical stability of (3,1)-chiral graphene nanoribbons. *ACS Nano* **15**, 5610–5617 (2021).
31. Perdew, J. P. & Zunger, A. Self-interaction correction to density-functional approximations for many-electron systems. *Phys. Rev. B* **23**, 5048–5079 (1981).
32. Hybertsen, M. S. & Louie, S. G. Electron correlation in semiconductors and insulators — band gaps and quasiparticle energies. *Phys. Rev. B* **34**, 5390–5413 (1986).
33. Lieb, E. H. Two theorems on the Hubbard model. *Phys. Rev. Lett.* **62**, 1201–1204 (1989).

# Methods

### Precursor synthesis and GNR growth

Full details of the synthesis and characterization of **1**–**5** are given in the Supplementary Information. N-6-ZGNRs were grown on Au(111) films on mica under UHV conditions. Atomically clean Au(111) surfaces were prepared through iterative $Ar^+$ sputter–anneal cycles. Sub-monolayer coverage of **1** on atomically clean Au(111) was obtained by sublimation at crucible temperatures of 460–470 K using a home-built Knudsen cell evaporator. After deposition the surface temperature was slowly ramped (≤2 K $min^{-1}$) to 475 K and held at this temperature for 30 min to induce the radical-step growth polymerization, then ramped slowly (≤2 K $min^{-1}$) to 650 K and held there for 30 min to induce cyclodehydrogenation.

### STM measurements

All STM experiments were performed using a commercial OMICRON low-temperature (LT)-STM held at $T = 4$ K using PtIr STM tips. STM tips were optimized for scanning tunnelling spectroscopy using an automated tip conditioning program[34]. d$I$/d$V$ measurements were recorded with CO-functionalized STM tips using a lock-in amplifier with a modulation frequency of 455 Hz and a modulation amplitude of $V_{RMS} = 11$ mV. d$I$/d$V$ point spectra were recorded under open feedback loop conditions. d$I$/d$V$ maps were collected under constant current conditions. BRSTM images were obtained by mapping the out-of-phase d$I$/d$V$ signal collected during a constant-height d$I$/d$V$ map at zero bias. Peak positions in d$I$/d$V$ point spectroscopy were determined by fitting the spectra with Lorentzian peaks. Each peak position is based on an average of approximately 90 spectra collected on 10 GNRs with 10 different tips, all of which were first calibrated to the Au(111) Shockley surface state.

### SPM tip-induced decoupling protocol

From the tunnelling setpoint ($I_t = 20$ pA, $V_s = 50$ mV), the STM tip is relocated to a position above the Au(111) substrate. Using an open-feedback loop, the bias voltage is ramped to ±2.5 V at a rate of approximately 100 mV $s^{-1}$ and the tunnelling current as a function of time is monitored. A monotonically increasing (decreasing) $I_t$ curve is used to ensure that a global tip change has not occurred. The process is repeated with the STM tip located above the GNR backbone. Discontinuous drops in the tunnelling current are used to indicate a successful decoupling event.

### Calculations

DFT calculations of GNR superlattices were performed in the LSDA as implemented in the Quantum ESPRESSO package[35], and the GW calculations were performed by the BerkeleyGW package[36]. Only freestanding GNRs (without substrate) were calculated. A supercell arrangement was used with 15 Å-wide vacuum regions carefully tested to avoid interactions between the GNR and its periodic images. We used norm-conserving pseudopotentials with a planewave energy cut-off of 60 Ry. The structure was fully relaxed within DFT-LSDA until the magnitude of the force on each atom was smaller than 0.02 eV $Å^{-1}$. All σ dangling bonds on the edges and the ends of the GNRs were capped by hydrogen atoms. A Gaussian broadening of 4 meV was used in the evaluation of the DOS and LDOS. In the GW calculation, the frequency-dependent screening is incorporated by the Hybertson–Louie generalized plasmon-pole (GPP) model[32], and self-consistency in the quasiparticle energy eigenvalues in the Green's function $G$ is performed.

### Stabilization of ZGNR edges through substitutional doping with N atoms

For any molecule, the total energy of formation $E_f$ is the energy required to break all covalent bonds in the molecule into the constituent isolated atoms and stripping all the electrons from the corresponding atomic nuclei. Conversely, this corresponds to the energy released upon assembling any molecular structure from the constituent isolated atomic nuclei and electrons. $E_f$ can be directly estimated using first-principles calculations with reference to a chosen standard state of the atoms (often the most stable molecular species of the element). A comparison of the energy of formation $\Delta E_f$ between two molecular species requires the application of an imaginary reaction that converts reactants $E_{f(reactants)}$ into products $E_{f(products)}$ along with the associated release of energy $\Delta E_f$.

$$\Delta E_f = \sum \upsilon E_{f(products)} - \sum \upsilon E_{f(reactants)} \quad (1)$$

Below, we show that the introduction of a superlattice of isoelectronic substitutional dopant atoms (one out of six $C_{sp2}$–H groups replaced by $N_{sp2}$ groups) along the edges of ZGNRs leads to an overall lowering of the energy of formation $\Delta E_f$. Following the imaginary reaction

$$6 - ZGNR + 2\ N \rightarrow N - 6 - ZGNR + 2C + 2H \quad (2)$$

and substituting in equation (1) we can determine the difference in the energy of formation $\Delta E_f$:

$$\Delta E_f = (E_{f(N-6-ZGNR)} + 2\mu_{(C-graphite)} + 2\mu_{(H-dihydrogen)}) - (E_{f(6-ZGNR)} + 2\mu_{(N-dinitrogen)}) \quad (3)$$

Using the same DFT functionals (local density approximation), cutoff energies, pseudopotentials, we calculated the energy of formation at $E_f$ at $T = 0$ K for the unit cell ($C_{70}N_2H_{10}$) of a nitrogen doped N-6-ZGNR ($E_{f(N\text{-}6\text{-}ZGNR)}$) and the identical size unit cell ($C_{72}H_{12}$) of the analogous carbon 6-ZGNRs ($E_{f(6\text{-}ZGNR)}$) . $\mu_{(C\text{-}graphite)}$, $\mu_{(H\text{-}dihydrogen)}$ and $\mu_{(N\text{-}dinitrogen)}$ are the calculated chemical potentials for carbon, hydrogen and nitrogen atoms in the lowest energy conformation of the element, respectively.

Substituting in equation (3) gives

$$\Delta E_f = (-852.07690\ Ry - 22.90529\ Ry - 2.27558\ Ry) - (-837.46377\ Ry - 39.78492\ Ry)$$
$$= \Delta E_f = -0.00908\ Ry = -0.124\ eV$$

The introduction of a superlattice of substitutional N-atom dopants along the edges of 6-ZGNRs leads to an overall lowering of the energy of formation $\Delta E_f$ of N-6-ZGNRs by −0.124 eV per unit cell compared to the structure of the all-carbon 6-ZGNR. Therefore, we conclude that N-6-ZGNR is energetically more stable than the all-carbon 6-ZGNR.

### Consideration of alternative origin of split nitrogen lone-pair flat bands

In the absence of a quantum exchange field or an external magnetic field, the up spin and down spin electrons residing in the highly localized trigonal planar N-atom lone-pair orbitals lining the edges of N-6-ZGNRs are degenerate (see Extended Data Fig. 7d). The strong hybridization of the spin-polarized edge state of as-grown N-6-ZGNRs with the Au(111) substrate largely quenches the local magnetic exchange field induced by a ferromagnetically ordered zigzag edge state. Splitting of the two spin-degenerate nitrogen flat bands can therefore only be observed once the local magnetic exchange field is restored as part of the SPM tip induced decoupling protocol. An alternative explanation that invokes a splitting of the spin-degenerate nitrogen flat bands solely by the interaction with an external magnetic field from either the SPM tip or the substrate can be excluded, as both the Au(111) surface and the CO-functionalized PtIr tips are non-magnetic.

## Data availability

DFT code with pseudopotentials and GW code can be downloaded from the Quantum Espresso (https://www.quantum-espresso.org) and the BerkeleyGW (https://www.berkeleygw.org) websites, respectively. We

used Quantum Espresso version 6.4.1 and BerkeleyGW version 2.1 for the theoretical calculations. All data presented in the main text and the supplementary information are available from the corresponding authors upon reasonable request.


34. Wang, S. K., Zhu, J. M., Blackwell, R. & Fischer, F. R. Automated tip conditioning for scanning tunnelling spectroscopy. *J. Phys. Chem. A* **125**, 1384–1390 (2021).
35. Giannozzi, P et al. QUANTUM ESPRESSO: a modular and open-source software project for quantum simulations of materials. *J. Phys. Condens. Mat.* **21**, 395502 (2009).
36. Deslippe, J et al. BerkeleyGW: a massively parallel computer package for the calculation of the quasiparticle and optical properties of materials and nanostructures. *Comput. Phys. Commun.* **183**, 1269–1289 (2012).



**Acknowledgements** This work was primarily funded by the US Department of Energy (DOE), Office of Science, Basic Energy Sciences (BES), Materials Sciences and Engineering Division under contract no. DE-AC02-05-CH11231 (Nanomachine program KC1203) (molecular design, surface growth, calculations and analyses of surface–GNR interactions). Research was also supported by the Office of Naval Research under award no. N00014-19-1-2503 (STM characterization), the National Science Foundation under grant nos. DMR-1839098 (image analysis) and DMR-1926004 (GW calculations), the Center for Energy Efficient Electronics Science ECCS-0939514 (magnetic modelling), and the Office of Naval Research MURI under award no. N00014-16-1-2921 (molecular synthesis, ab initio DFT calculations). This research used resources of the National Energy Research Scientific Computing Center (NERSC), a US Department of Energy Office of Science User Facility operated under Contract No. DE-AC02-05-CH11231. Computational resources were also provided by the National Science Foundation through XSEDE resources at the NICS. R.E.B. acknowledges support through a National Science Foundation Graduate Research Fellowship under grant DGE-11064000. We thank the College of Chemistry for use of resources at their NMR facility, and we thank their staff for assistance. Instruments in CoC-NMR are supported in part by NIH S10OD024998.


**Author contributions** R.E.B., F.Z., S.G.L and F.R.F. initiated and conceived the research. E.B., I.P. and F.R.F designed, synthesized, and characterized the molecular precursors. R.E.B., S.W., J.Z., A.D. and F.R.F. performed on-surface synthesis and STM characterization and analysis. F.Z., Y.-L.L. and S.G.L. performed DFT and GW calculations as well as theoretical analyses, and assisted with data interpretation. R.E.B., F.Z., S.G.L. and F.R.F. wrote the manuscript. All authors contributed to the scientific discussion.

**Competing interests** The authors declare no competing interests.

**Additional information**


**Supplementary information** The online version contains supplementary material available at https://doi.org/10.1038/s41586-021-04201-y.



**Correspondence and requests for materials** should be addressed to Steven G. Louie or Felix R. Fischer.



**Peer review information** *Nature* thanks Rémy Pawlak, Levente Tapaszto and Daniel Sanchez-Portal for their contribution to the peer review of this work.

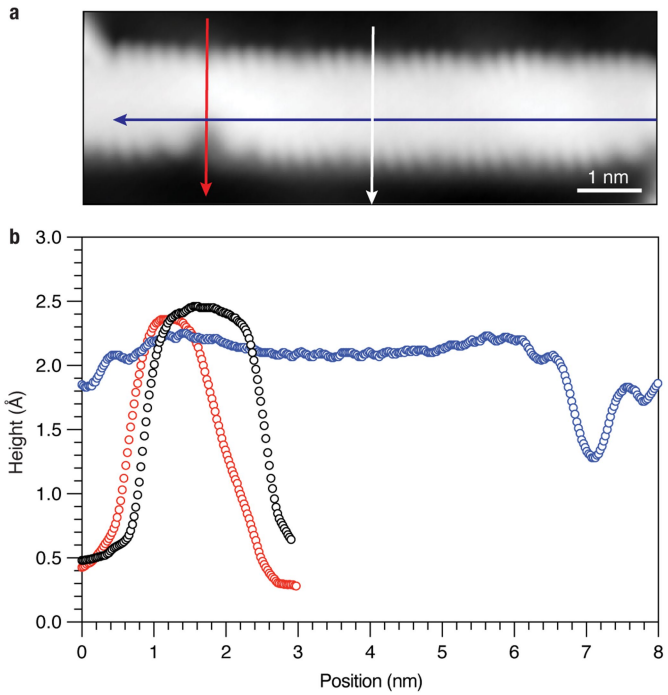


**Extended Data Fig. 1 | Height profiles of N-6-ZGNRs on Au(111). a**, STM topographic image of N-6-ZGNR on Au(111) ($V_s$ = 50 mV, $I_t$ = 20 pA; CO-functionalized tip). **b**, Height profile recorded along the arrows marked in **a**.

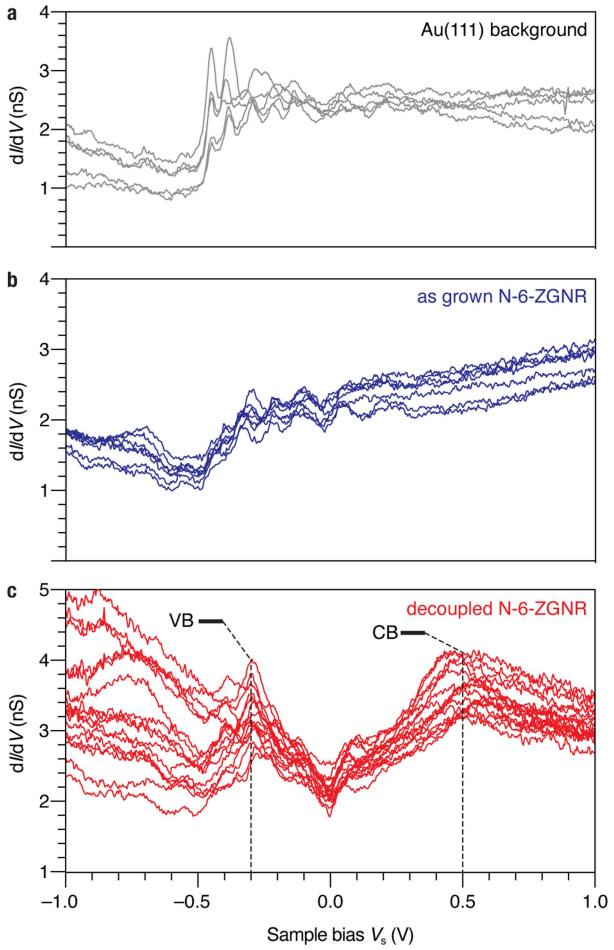


**Extended Data Fig. 2 | d*I*/d*V* point spectroscopy of N-6-ZGNRs on Au(111).** **a**, d*I*/d*V* point spectra collected on bare Au(111) ($V_{ac}$ = 11 mV, $f$ = 455 Hz). **b**, d*I*/d*V* point spectra collected on as grown segments of N-6-ZGNRs. **c**, d*I*/d*V* point spectra collected on decoupled segments of N-6-ZGNRs following the SPM tip-induced decoupling protocol.

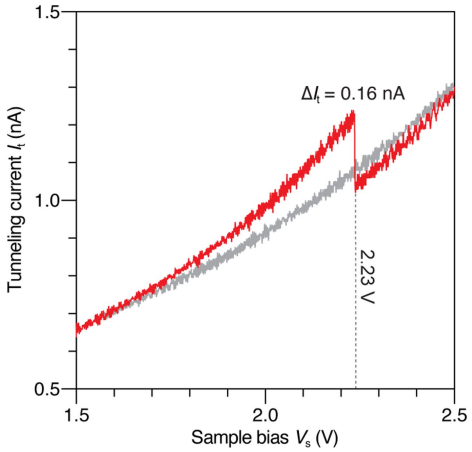


**Extended Data Fig. 3 | Tip induced decoupling of N-6-ZGNRs.** $I_t/V_s$ plot showing in red the positive voltage sweep ($V_s$ = +1.50 V to $V_s$ = +2.50 V) used during the decoupling procedure. The respective return sweep ($V_s$ = +2.50 V to $V_s$ = +1.50 V) is depicted in grey and shows the irreversible shift in the tunnelling current $I_t$.

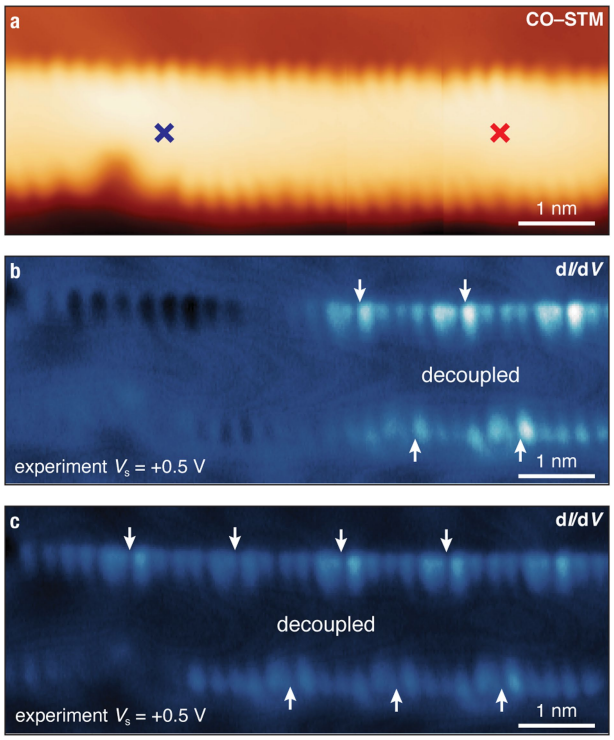


**Extended Data Fig. 4 | Tip-induced decoupling of magnetic edge states in N-6-ZGNRs. a**, Topographic image of a fully cyclized N-6-ZGNR segment recorded with CO-functionalized STM tip. **b**, Constant-current d*I*/d*V* map recorded at a voltage bias of $V_s$ = +0.5 V of N-6-ZGNR segment following tip-induced decoupling using a positive voltage sweep from $V_s$ = 0.0 V to $V_s$ = +2.5 V at the position marked by a red cross in **a** ($V_{ac}$ = 11 mV, $I_t$ = 200 pA, $f$ = 455 Hz, CO functionalized tip). **c**, Constant-current d*I*/d*V* map recorded at a voltage bias of $V_s$ = +0.5 V of N-6-ZGNR segment following tip-induced decoupling using a negative voltage sweep from $V_s$ = 0.0 V to $V_s$ = −2.5 V at the position marked by a blue cross in **a** ($V_{ac}$ = 11 mV, $I_t$ = 200 pA, $f$ = 455 Hz, CO functionalized tip). Arrows mark the position of selected N-atom along the edge of the N-6-ZGNR.

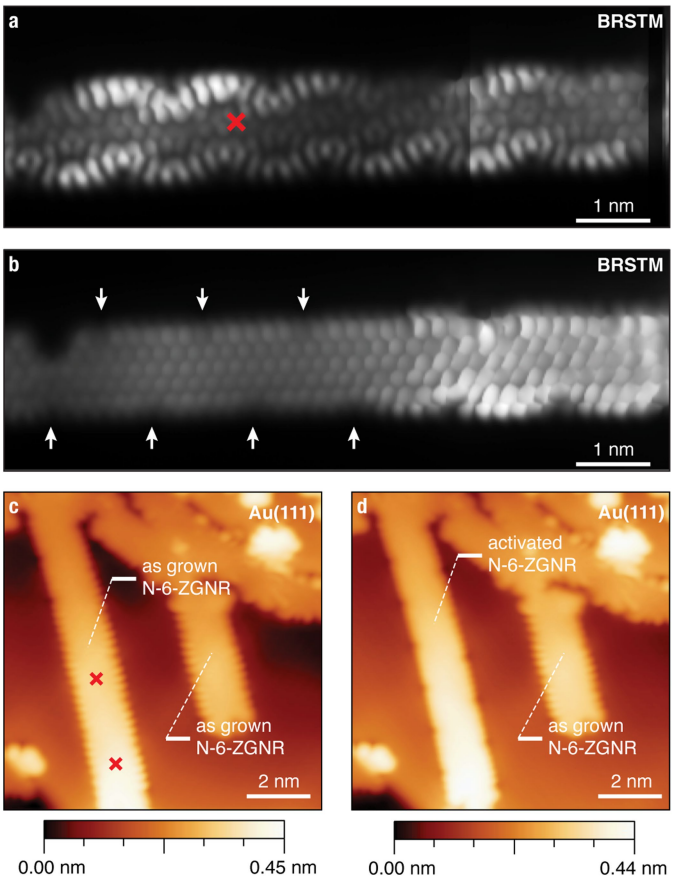


**Extended Data Fig. 5 | Bond resolved imaging of decoupled N-6-ZGNRs.** **a**, Constant-height BRSTM image of a N-6-ZGNR segment from ($V_s$ = 0 mV, modulation voltage $V_{ac}$ = 11 mV, modulation frequency $f$ = 455 Hz). **b**, Constant-height BRSTM image of the N-6-ZGNR segment in **a** following tip-induced decoupling using a positive voltage sweep from $V_s$ = 0.0 V to $V_s$ = +2.5 V at the position marked by a red cross in **a** ($V_s$ = 0 mV, $V_{ac}$ = 11 mV, $f$ = 455 Hz). Arrows mark the position of selected N-atom along the edge of the N-6-ZGNR. **c**, STM topographic image of as-grown N-6-ZGNRs with CO-modified tip. **d**, STM topographic image of N-6-ZGNR after decoupling the GNR on the left. ($V_s$ = 50 mV, $I_t$ = 20 pA).

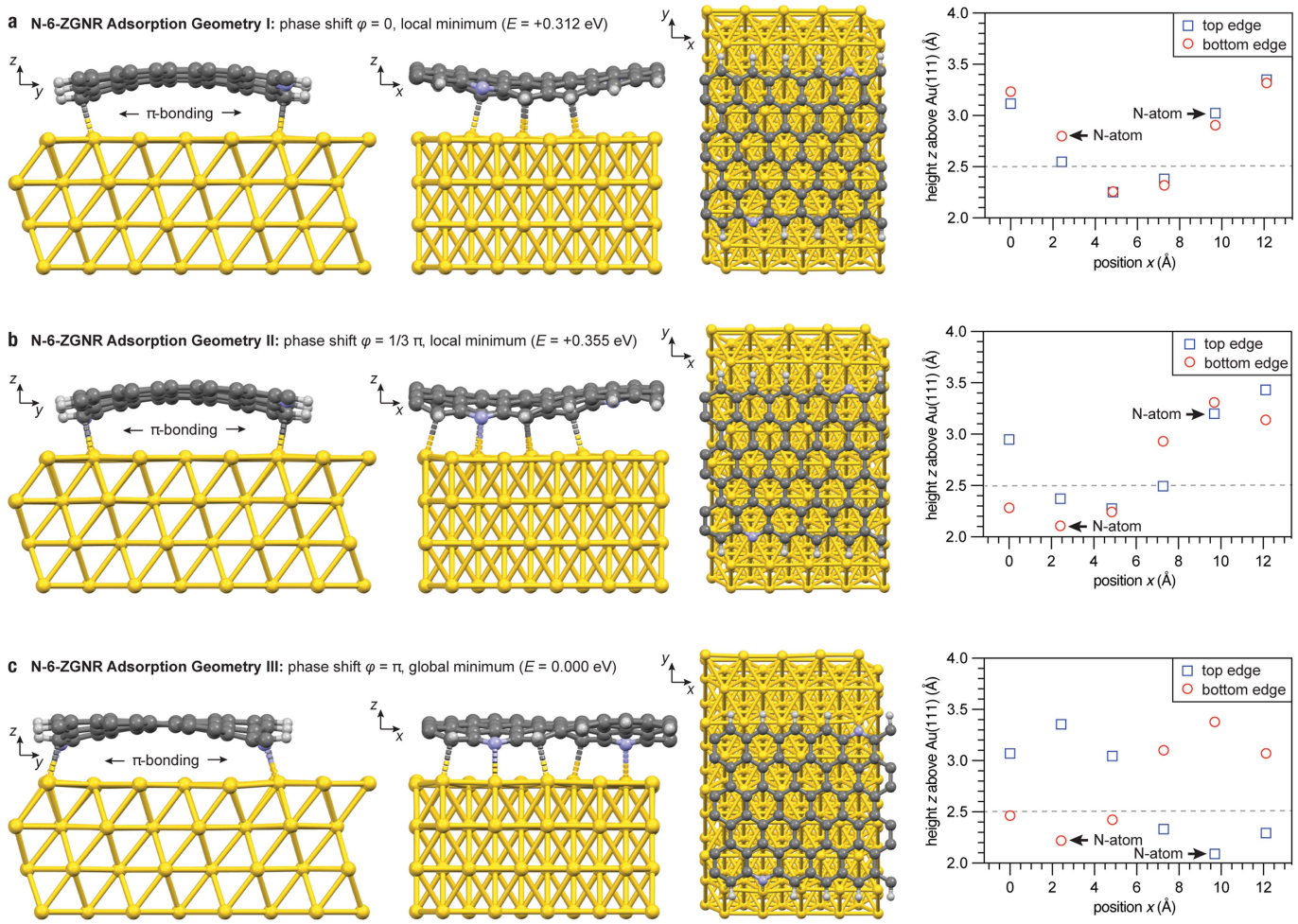


**Extended Data Fig. 6 | Calculated adsorption geometries of N-6-ZGNRs on Au(111). a**, Local minimum Adsorption Geometry I ($E$ = +0.312 eV). Four C-atoms per unit cell interact through π-bonding (< 2.5 Å) with the Au(111) surface. The corrugation on opposing zigzag edges is in phase ($\varphi = 0$). **b**, Local minimum Adsorption Geometry II ($E$ = +0.355 eV). Five C-atoms and one N-atom per unit cell interact through π-bonding (< 2.5 Å) with the Au(111) surface. The corrugation on opposing zigzag edges is phase shifted by $\varphi = 1/3\pi$. **c**, Global minimum Adsorption Geometry III ($E$ = +0.000 eV). Four C-atoms and two N-atoms per unit cell interact through π-bonding (< 2.5 Å) with the Au(111) surface. The corrugation on opposing zigzag edges is phase shifted by $\varphi = \pi$. All calculations performed with ultrasoft pseudopotentials and 40 Ry cut-offs.

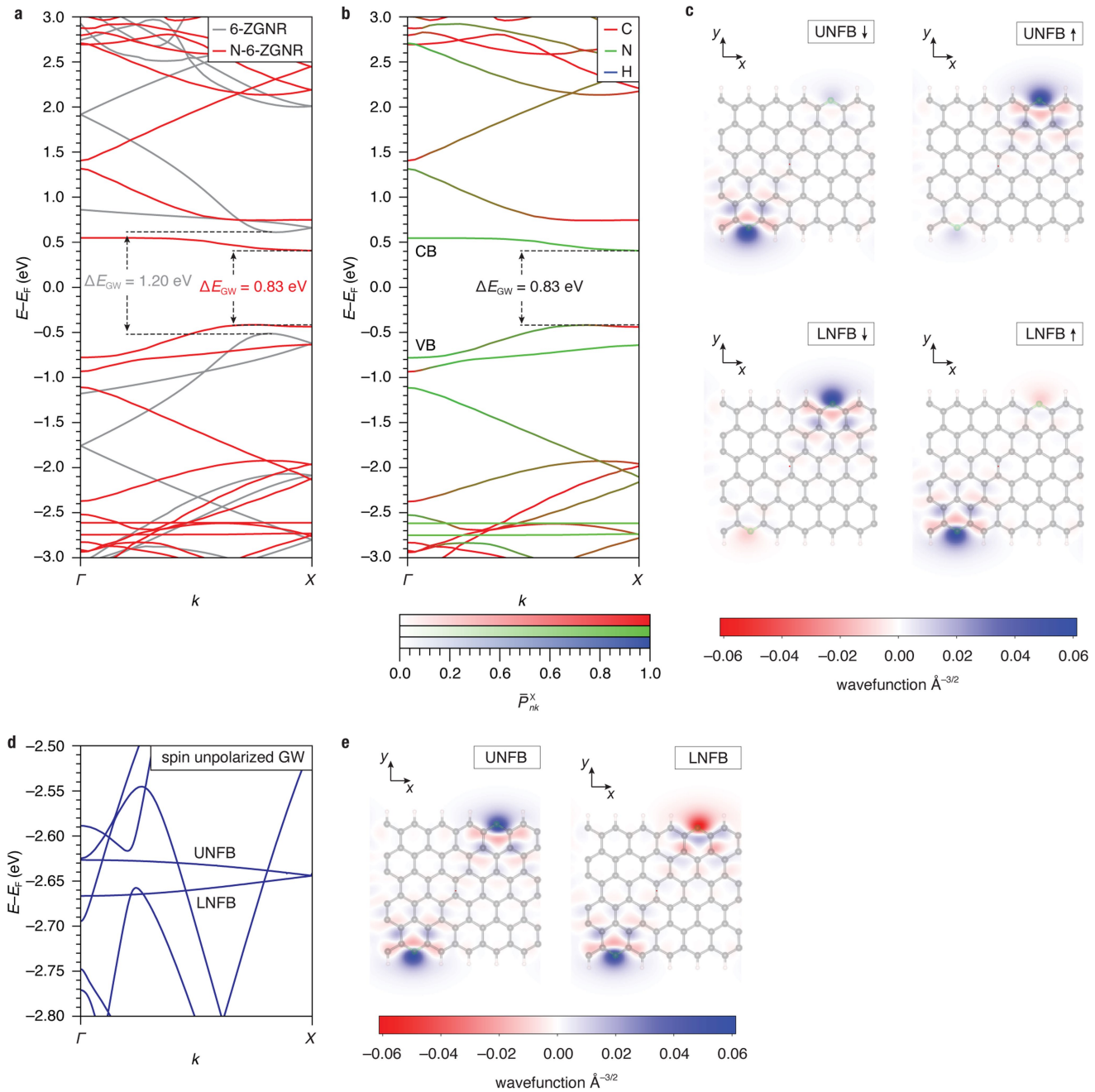


**Extended Data Fig. 7 | Electronic structure of 6-ZGNR and N-6-ZGNRs. a**, GW band structure of freestanding 6-ZGNR (grey) and N-6-ZGNR (red) calculated using the same dimension unit cell. **b**, GW band structure of a freestanding N-6-ZGNR. The colour code shows the normalized contributions from C-atoms, N-atoms, and H-atoms to the wavefunction of each state. The number of $p_z + \sigma$ orbitals for C, N, and H atoms are 280, 8, and 10 per unit cell, respectively. The wavefunction projection of the state in the $n^{th}$ band and at wavevector $k$ to the C, N, and H atoms is described by $P_{nk}^{C}$, $P_{nk}^{N}$, and $P_{nk}^{H}$, respectively. We define the normalized percentage weight $P_{nk}^{C}$, $P_{nk}^{N}$, and $P_{nk}^{H}$ as the wavefunction projection on the C, N, and H atoms per atom in the unit cell: $\bar{P}_{nk}^{C} = P_{nk}^{C}/280$, $\bar{P}_{nk}^{N} = P_{nk}^{N}/8$, $\bar{P}_{nk}^{H} = P_{nk}^{H}/10$. The scale bar defines the mapping between the colour scale and the normalized percentage weight. **c**, Spatial distribution of the calculated spin polarized wavefunction for UNFB and LNFB. **d**, Spin unpolarized GW band structure of a freestanding N-6-ZGNR (with DFT within the local density approximation (LDA) as the starting point). In the spin unpolarized calculation the UNFB and LNFB form narrow non-splitting bands with a total band width smaller than 50 meV. **e**, Spatial distribution of the calculated spin unpolarized wavefunction for UNFB and LNFB.

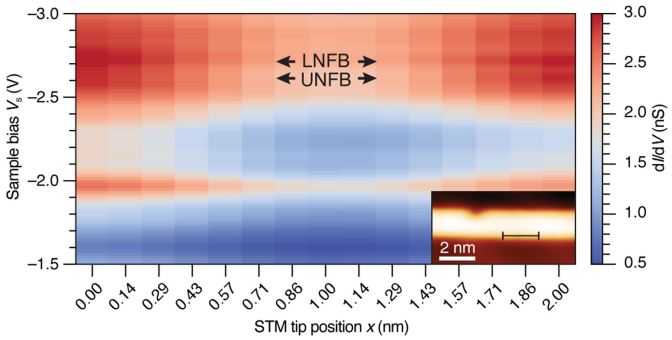


**Extended Data Fig. 8 | Spatial localization of spin split low-lying nitrogen dopant flat band states.** Waterfall plot of d*I*/d*V* point spectra collected along a line marked in the inset long the edge of a N-6-ZGNR ($V_{ac}$ = 11 mV, $f$ = 455 Hz). When the STM tip is located immediately above the position of a nitrogen dopant atom the d*I*/d*V* point spectra show two characteristic peaks centred at $V_s = -2.60 \pm 0.02$ V and $V_s = -2.70 \pm 0.02$ V, corresponding to the UNFB and LNFB states, respectively.

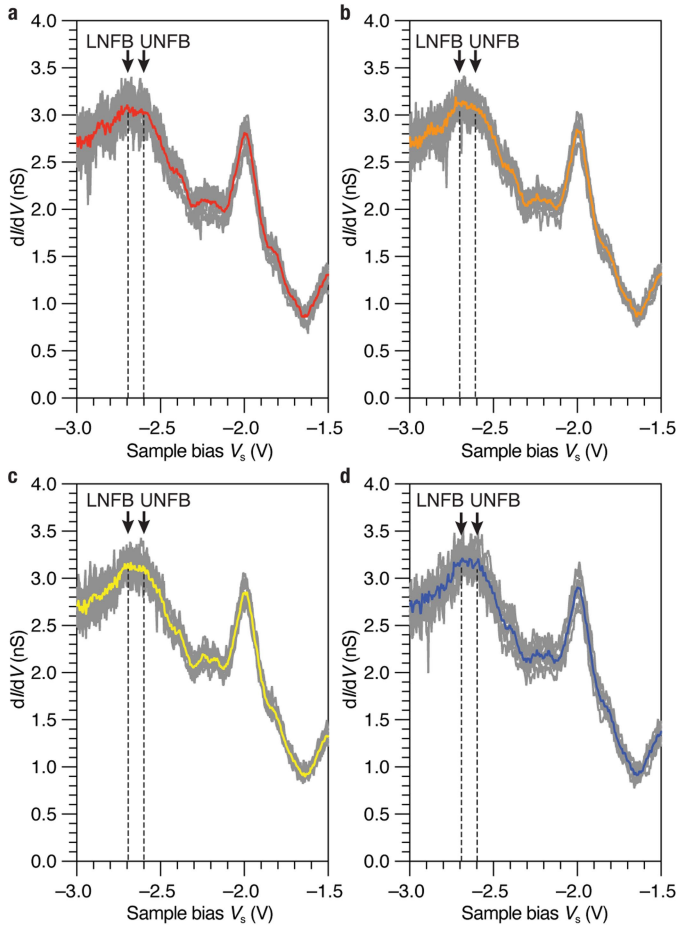


**Extended Data Fig. 9 | d*I*/d*V* point spectroscopy of spin split low-lying nitrogen dopant flat band states.** d*I*/d*V* point spectroscopy recorded on four different decoupled N-6-ZGNR/Au(111) at the position above the N atoms. Ten d*I*/d*V* point spectra were collected at each position (grey). The respective averaged d*I*/d*V* point spectra are highlighted in red, orange, yellow, and blue (spectroscopy: $V_{ac} = 11\,\text{mV}$, $f = 455\,\text{Hz}$).

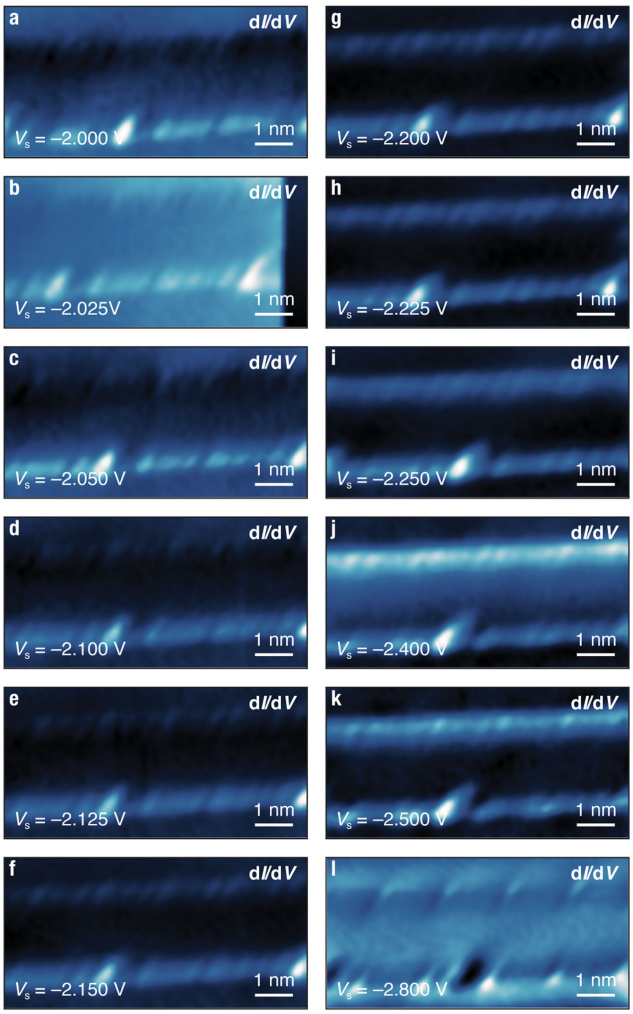


**Extended Data Fig. 10 | Constant-current d*I*/d*V* maps of decoupled N-6-ZGNR.** d*I*/d*V* maps recorded at voltage biases of **a**, $V_s$ = −2.000 V, **b**, $V_s$ = −2.025 V, **c**, $V_s$ = −2.050 V, **d**, $V_s$ = −2.100 V, **e**, $V_s$ = −2.125 V, **f**, $V_s$ = −2.150 V, **g**, $V_s$ = −2.200 V, **h**, $V_s$ = −2.225 V, **i**, $V_s$ = −2.250 V, **j**, $V_s$ = −2.400 V, **k**, $V_s$ = −2.500 V, and **l**, $V_s$ = −2.800 V ($V_{ac}$ = 11 mV, $I_t$ = 2 nA, $f$ = 455 Hz).